PAPER

Check for updates

Sulfur-doped CoFe$_2$O$_4$ nanopowders for enhanced visible-light photocatalytic activity and magnetic properties†

Rong Li, [ID]* Chencen Sun, Jia Liu and Qiang Zhen*

Magnetically recoverable sulfur-doped CoFe$_2$O$_4$ nanopowders were used as photocatalyst for degradation of oxytetracycline (OTC) under visible light in aqueous solution. S doped CoFe$_2$O$_4$ nanopowders synthesized by a simple calcining process were characterized by XRD, TEM, VSM, FT-IR, UV-vis DRS and XPS. The results showed that introducing of S element in CoFe$_2$O$_4$ crystal structure narrowed its band gap and increased visible light absorption. 0.3 S-CoFe$_2$O$_4$ exhibited the highest magnetic property and photocatalytic activity. The maximum photocatalytic conversion ratio of OTC reached 90.4% at pH = 8.5 after 5 h irradiation. During photocatalytic process, seven intermediate products were detected, and based on that a detailed degradation path way of OTC was proposed.

1. Introduction

Antibiotics have been widely used as antibacterial agents in human and veterinary medicine for the treatment of bacterial infections.[1,2] Because of their poor adsorption by human beings or live stocks and chemical stability, some of these antibiotics, such as tetracyclines (TCs), have been accumulating in the aquatic environment.[3,4] Antibiotic residues are potentially dangerous to ecosystems, especially to human health through drinking water and the food chain. Among the TCs family, oxytetracycline (OTC) is one of the most frequently detected tetracyclines in water bodies and sediments in many countries, which is difficult to removal by conventional water treatment process.[5,6]

Photocatalytic oxidation technology has been considered as an effective way to remove the organic pollutants in aqueous solution, due to its energy saving, environmental friendly performance and no secondary pollution.[7] Many photocatalysts have been developed for antibiotic degradation under solar and visible light.[8,9] However, the recoverability and photocatalytic activity under visible light of common photocatalysts need to be further improved for practical application.

Spinel ferrites (MFe$_2$O$_4$, M = metal cation) can be easily collected due to their great magnetic property,[10–12] and excited under visible light irradiation due to their relatively narrow

bandgap.[11,13] Therefore, it is considered as potential photocatalyst in eliminating various organic pollutants.[14,15] Among these materials, CoFe$_2$O$_4$ attracts more attention due to its moderate magnetic performance at room temperature and good chemical stability.[16] It is often composited with other semiconductor materials such as TiO$_2$, WO$_3$ and C$_3$N$_4$, or conducting materials such as graphene, oxidized graphene and carbon nanotube, in order to improve the photocatalytic degradation performance.[17–19] However, the synthetic process of these composites is complex, and the magnetism may be reduced due to introduce of nonmagnetic components. Non-metal doping is an effective way to modify common photocatalysts, such as TiO$_2$, which has been reported in many literatures.[20,21] But there are few references about improving photocatalytic performance of CoFe$_2$O$_4$ by non-metal doping. Although Cao *et al.* have reported that the magnetic property of CoFe$_2$O$_4$ is improved by doped nonmetal sulfur,[22] the effects of doped S element on photocatalytic performance has not been involved.

Therefore, this work attempted to realize photocatalytic degradation of OTC under visible light using magnetically recoverable S doped CoFe$_2$O$_4$ nanopowders as photocatalysts. The S doped CoFe$_2$O$_4$ nanopowders were synthesized and characterized by XRD, TEM, VSM, FT-IR, UV-vis DRS and XPS. The effects of S on photocatalytic activity and magnetic property were investigated to optimize the concentration of S. The photocatalytic degradation of OTC at different initial pH was studied, as well as the photocatalytic stability. Then the intermediate products during photocatalytic process were determined to deduce the degradation path way of OTC. At last, the photocatalytic mechanism was further investigated based on research results.

Nanoscience and Technology Research Center, Shanghai University, Shanghai 200444, China. E-mail: lirong376@hotmail.com; qzhen@staff.shu.edu.cn; Tel: +86 21 66137276

2. Experiment section

2.1 Synthesis

$CoFe_2O_4$ and sulfur-doped $CoFe_2O_4$ (S-$CoFe_2O_4$) nanoparticles have been synthesized as reported in literature.[22] To obtain $CoFe_2O_4$ nanopowders, 4.848 g $Fe(NO_3)_3 \cdot 9H_2O$, 1.746 g $Co(NO_3)_2 \cdot 6H_2O$ were dissolved in dimethyl formamide (DMF, 15 mL), then this solution was put into an alumina crucible and calcined at 700 °C for 2 hours with the heating rate of 1 °C min^{-1} in air. S-$CoFe_2O_4$ nanopowders were synthesized using the same method by adding thiourea in the DMF solution. The concentration of thiourea was in a range of 0.1–0.5 mol L^{-1} to adjust S content in S-$CoFe_2O_4$.

2.2 Characterization

The phases of obtained $CoFe_2O_4$ and S doped $CoFe_2O_4$ nanopowders were identified by X-ray diffraction (XRD, Rigaku, D/MAX2500V) using Cu-K_α ($\lambda = 0.15418$ nm) radiation. The XRD data were collected in the range of 20–80° with a scanning rate of 8° min^{-1}. Vibrating sample magnetometer (VSM, China Trend Limited, Lakeshore 7407) was used to measure the magnetic properties of all samples.

The morphologies of both $CoFe_2O_4$ and 0.3 mol L^{-1} S doped $CoFe_2O_4$ (0.3S-$CoFe_2O_4$) nanopowders were observed using the transmission electron microscope (TEM, Jeol, JEM-2100F) equipped with energy-dispersive X-ray (EDX). The Fourier transfer infrared spectroscopy (FT-IR) of S-$CoFe_2O_4$ nanopowders was recorded using an infrared spectrometer (FT-IR, Nicolet, AVATAR370), and compared with $CoFe_2O_4$ nanopowders. The UV-vis diffuse reflectance spectra of both nanopowders were recorded by UV-vis spectrometer (DRS, Persee, TU-1901) with an integrating sphere.

The binding energies of Co, Fe, S of $CoFe_2O_4$ and 0.3S-$CoFe_2O_4$ were determined by X-ray photoelectron spectroscopy (XPS, Thermofisher Scientific, ESCALAB 250Xi). The zeta potential (Zeta) of sample was measured with a nanoparticles and potential analyzer (Zeta, Malvern lnstruments, Zetasizer 3000HS).

2.3 Photocatalytic degradation measurement

The photocatalytic experiments were carried out as described in our previous work.[5] The experimental procedure was as follows: 70 mg of photocatalyst was first suspended in 70 mL OTC aqueous solution (80 mg L^{-1}, $C_{22}H_{24}N_2O_9 \cdot HCl$: 95% purity, Aladdin Chemistry Co., Ltd, Shanghai, China) in a quartz tube, then stirred at 900 rpm continuously for 1 h before light irradiation to ensure that the photocatalyst surface was saturated with OTC molecules. The mixture was irradiated under a 300 W iodine tungsten lamp, which located 25 cm away from the quartz tube. All the tests were performed at room temperature. At given time intervals of irradiation, 5 mL of the suspension was filtered and the residual concentration of OTC was monitored using a UV-Vis spectrophotometer (Cary 5000 UV-Vis-NIR, Agilent) at 365 nm. The photocatalytic conversion ratio (PCR) of OTC was estimated according to the formula:

$$PCR = (1 - C_t/C_0) \times 100\% \qquad (1)$$

where C_t (mg L^{-1}) is the solution concentration of OTC after irradiation at any time, and C_0 is the initial concentration of OTC solution. C can be calculated through the corresponding absorbance according to the standard curve. The total organic carbon (TOC) in OTC aqueous solution after photocatalytic was measured using TOC Analyzer Total (TOC, Analytik Jena Ag, N/C 2100).

The photocatalytic stability of 0.3S-$CoFe_2O_4$ nanopowders was investigated by recycling tests at room temperature. In these experiments, 70 mg of photocatalysts were suspended in 70 mL OTC (initial concentration of 80 mg L^{-1}) aqueous solution, and the pH of solution was adjusted to 8.5 for best performance. After each cycle of test, 0.3S-$CoFe_2O_4$ photocatalyst was separated from OTC solution in an external magnetic field and washed with water, dried at 120 °C for 4 h, then used for the next cycle. The process was repeated five times.

2.4 Photocatalytic degradation mechanism of OTC

The photocatalyst degradation intermediate products of OTC were detected by high performance liquid phase chromatography coupled with low resolution electrospray ionization mass spectrometry (LC/MSD SL, Agilent 1100 Series G1956B LC/MSD SL).

In order to determine ˙OH production, 200 mM NaOH and 60 mM terephthalic acid (TA) were added in the photocatalytic suspended solution. This solution was stirred in the dark for 1 h, then illuminated under a high pressure 300 W iodine tungsten lamp for 3 h. After centrifuged, the solution was analyzed on a fluorescence spectrometer (LS 55, PerkinElmer, UK) to record the fluorescence signal of the generated highly fluorescent product TAOH (excitation, $\lambda_{exc} = 312$ nm; the scanning speed, $v = 200$ nm min^{-1}; widths of the excitation slit and the emission slit, $d = 5$ nm).

The trapping experiment for hydroxyl radicals and holes on the photocatalytic photodegradation of OTC were carried out by using tert-butanol (t-BuOH, 0.1 M, radical scavenger) and ethylenediaminetetraacetic acid disodium salt (EDTA-2Na, 0.1 M, hole scavenger) as scavenger. For study the role of superoxide radicals, carbon tetrachloride (CCl_4 1 mM) was added under sparging N_2. The followed experimental process was carried out as mentioned above.

3. Results and discussions

3.1 Characterization of S-$CoFe_2O_4$ nanopowders

3.1.1 XRD analysis. Fig. 1(a) presents the XRD patterns of the nanopowders with different S concentrations. When the S concentration increased for 0 to 0.3 mol L^{-1}, the samples exhibited single cubic phase of $CoFe_2O_4$ (JCPDS card no. 22-1086). However, further increasing the S concentration to 0.5 mol L^{-1}, an extraneous α-Fe_2O_3 (JCPDS card no. 33–0664) impurity phase was observed. Fig. 1(b) shows that the d value of (311) diffraction peak slightly increases with increasing S
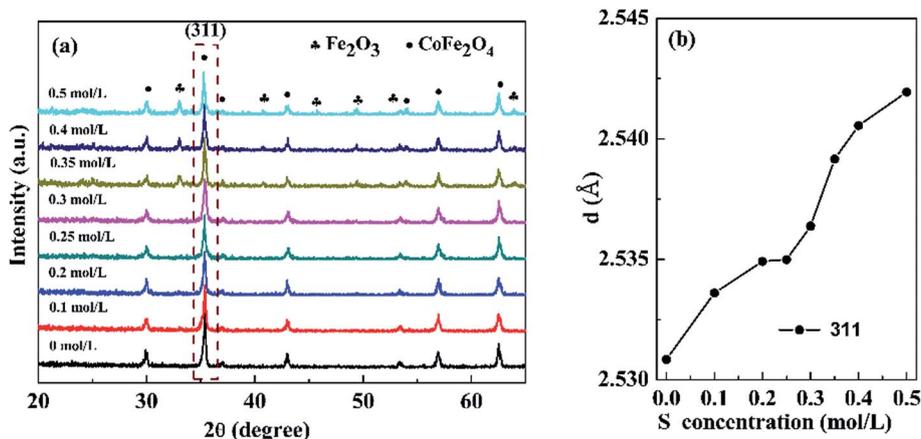
Fig. 1 (a) XRD patterns of the sample with different S concentrations, (b) the *d* value of (311) diffraction peaks varied with S concentrations.

concentration due to expansion of the lattice. The results indicated that S was effectively incorporated into the $CoFe_2O_4$ nanopowders.

3.1.2 Magnetism. Fig. 2(a) shows the magnetic hysteresis (M − H) loops of pure $CoFe_2O_4$ and S doped $CoFe_2O_4$. All samples followed typical room-temperature ferromagnetic behavior. The S concentration dependence of the magnetic saturation (M_S) of all products is given in Fig. 2(b). The M_S monotonically increased with S concentration rising from 0 to 0.3 mol L^{-1}, then decreased with further rising S concentration to 0.5 mol L^{-1} 0.3S-$CoFe_2O_4$ exhibited the highest magnetic saturation (M_S) of 69.1 emu g^{-1}. The inset camera photo shows that 0.3S-$CoFe_2O_4$ is easily separated from the solution by a magnet.

As reported in literature,[22] the increase of M_S was attributed to the migration of Co^{2+} ions from the B site to the A site, and hence the migration of Fe ions from the A site to the B site in small amounts caused by the inclusion of thiourea during the calcining process. In addition, the increase of average crystalline size (calculated using Scherrer equation form XRD, shown in Table 1) might also cause the increase of M_S. The decrease of M_S with S concentration above 0.3 mol L^{-1} was mainly caused by the presence of non-magnetic α-Fe_2O_3, which led to the relative reduction of magnetic $CoFe_2O_4$.

Table 1 The average crystalline size calculated by Scherrer equation with different S concentration

S content (mol L^{-1})	0	0.1	0.2	0.25	0.3
Average crystalline size (nm)	29.06	32.39	35.65	39.54	42.09

3.1.3 TEM analysis. Fig. 3(a) and (b) shows the representative TEM image of $CoFe_2O_4$ and 0.3S-$CoFe_2O_4$ nanopowders, respectively. It can be seen that the pure $CoFe_2O_4$ and 0.3S-$CoFe_2O_4$ are composed of uniform microspheres with size of 20–40 nm, but agglomerations also existed.

Fig. 3(c) shows a typical HAADF-STEM image of 0.3S-$CoFe_2O_4$ nanopowders, the distribution of each element has been studied by STEM mapping (shown in Fig. 3(d)). Co, Fe, O were all distributed uniformly throughout the 0.3S-$CoFe_2O_4$ nanoparticle. However, the signal points of S element are fewer, because of the lower concentration of S than other elements. It seems that elemental S may thus have been absorbed near gap or edge of $CoFe_2O_4$.

3.1.4 FT-IR and UV-vis absorption spectra. FT-IR spectra and UV-vis absorption spectra of pure $CoFe_2O_4$ and 0.3S-$CoFe_2O_4$ are shown in Fig. 4(a) and (b), respectively. In Fig. 4(a), compared with pure $CoFe_2O_4$, the spectrum of 0.3S-$CoFe_2O_4$
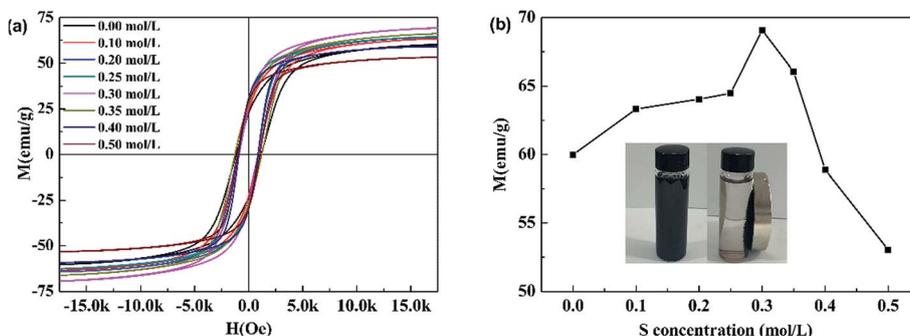

Fig. 2 (a) Magnetization curves at 296 K, (b) S concentration-dependence of M_S for the corresponding samples, inset shows the magnetic separation process of S-$CoFe_2O_4$.
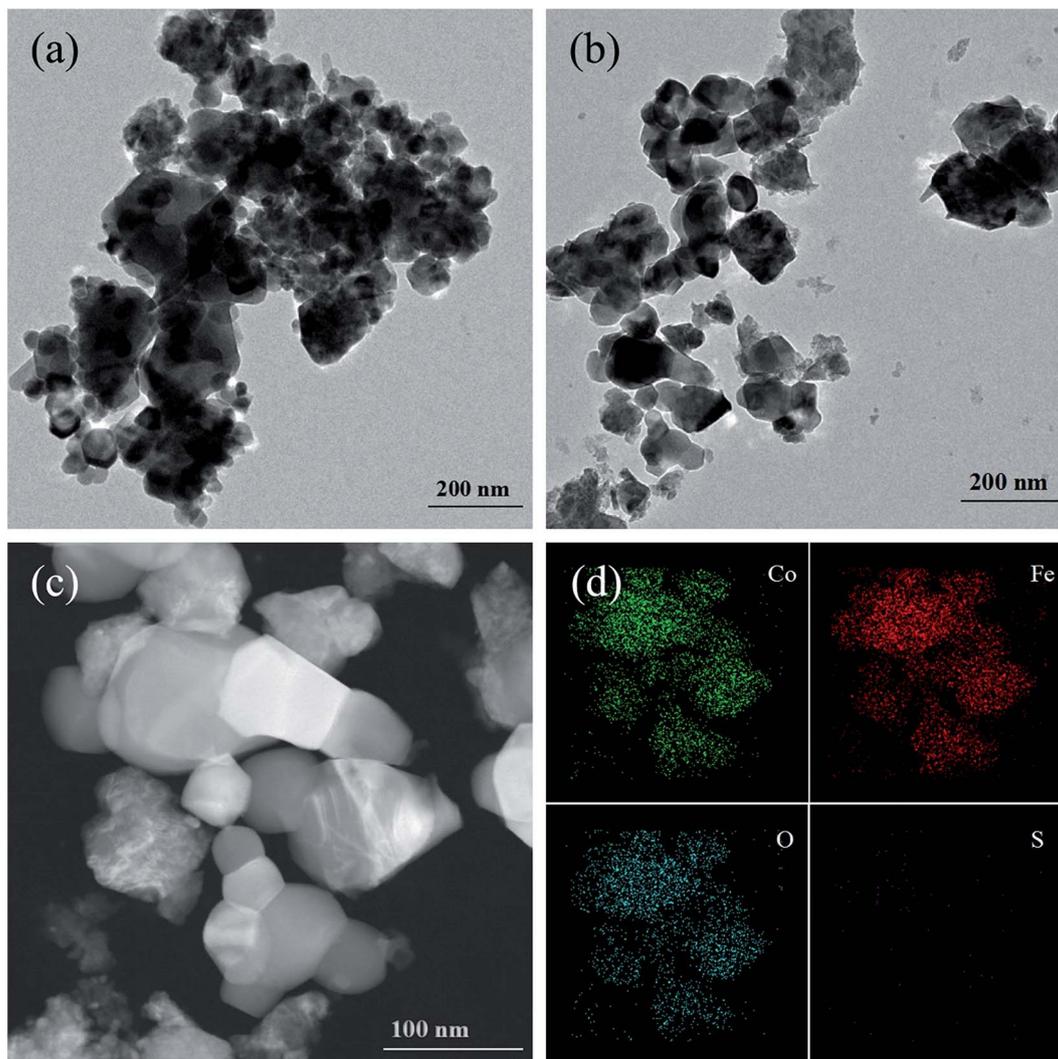
Fig. 3 TEM image of (a) $CoFe_2O_4$, (b) 0.3S-$CoFe_2O_4$, HTEM image of (c) 0.3S-$CoFe_2O_4$, (d) EDX-mapping of 0.3S-$CoFe_2O_4$ nanoparticles.

shows a distinguishing divisive band at about 1123 cm^{-1}, which assigns to S=O or S–O bond in sulfated oxides.[23,24] In Fig. 4(b), it can be seen that both $CoFe_2O_4$ and 0.3 S-$CoFe_2O_4$ exhibit stronger absorption in visible light region compared with TiO_2 nanopowders (P25). As expected, 0.3S-$CoFe_2O_4$ has stronger light absorption intensity than pure $CoFe_2O_4$ at the range of 540–800 nm. From the inset in Fig. 4(b), the band gap of S-$CoFe_2O_4$ is around 1.25 eV, bit less than that of $CoFe_2O_4$ (1.4 eV). The stronger absorption in visible light area and narrowed bandgap of 0.3S-$CoFe_2O_4$ were attributed to the introduction of S atoms in the lattice of $CoFe_2O_4$.

3.1.5 X-ray photoelectron spectroscopy. XPS is used to analyze the elemental composition of the prepared 0.3S-$CoFe_2O_4$. The full scanned XPS spectra demonstrate the existing of elements of Co, Fe, S and O (Fig. 5(a)), which is corresponding to the EDX analysis. The high-resolution XPS spectrum of S 2p is shown inset in Fig. 5(a), two individual peaks at 168.7 eV and 170.2 eV, which can be attributed to the oxidized S species,[22,23] corresponding to the result from FT-IR. Combined with the increase of the interplanar spacing from XRD patterns,

it suggested that S atoms might enter into the octahedral gap of $CoFe_2O_4$ lattice instead of replacing O atoms as expected.

As discerned from the XPS spectrum of Co 2p (Fig. 5(b)), two main peaks at 781.00 eV and 797.00 eV correspond to Co 2p$_{3/2}$ and Co 2p$_{1/2}$, respectively.[25] Besides, two satellite peaks at 786.71 eV and 804.50 eV relate to shake-up type of Co 2p$_{3/2}$ and Co 2p$_{1/2}$ edge, confirming the +2 oxidation state of the Co elements in 0.3S-$CoFe_2O_4$ nanopowders. In the XPS spectrum of Fe 2p (Fig. 5(c)), the peaks at 710.88 eV and 724.28 eV correspond to Fe 2p$_{3/2}$ and Fe 2p$_{1/2}$, respectively. The characteristic satellite peak between these two peaks at 717.73 eV suggests the +3 oxidation state of the Fe element.[26] The corresponding O 1s spectrum is given in Fig. 5(d), peaks at 530.0 and 532.3 eV represent the lattice oxygen of metal oxides and chemisorbed oxygen (M − OH).[27,28]

3.2 Photocatalytic degradation activity tests

3.2.1 Effect of S concentration on photocatalytic activity. Fig. 6(a) shows typical UV-vis spectra changes of OTC solution
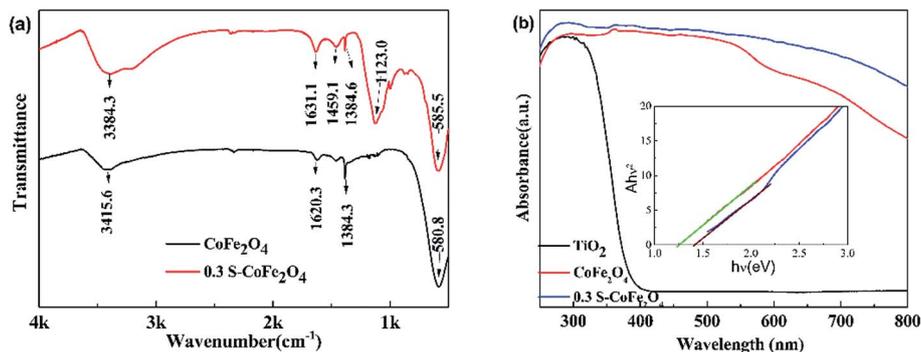
Fig. 4 (a) FT-IR spectra (b) UV-vis DRS of $CoFe_2O_4$ and $0.3S-CoFe_2O_4$, the inset shows plot of transferred Kubelka–Munk vs. energy of the light absorbed.

with reaction time using $0.3S-CoFe_2O_4$ as photocatalyst. The result showed that the adsorption peak of OTC around 354 nm significantly reduced with increasing irradiation time in 5 h. Fig. 6(b) gives the dependence of S concentration on PCR of OTC under visible light. The PCR firstly increased when S concentration was increased from 0 to 0.3 mol L^{-1}, then decreased with further increasing S concentration to 0.5 mol L^{-1} due to the formation of α-Fe_2O_3. $0.3S-CoFe_2O_4$ exhibited the highest photocatalytic activity under visible light, the PCR of OTC reached to 83% after 5 h irradiation. And in our tests (Fig. 2(b)), the $0.3S-CoFe_2O_4$ also exhibited highest magnetic property. Thus, $0.3S-CoFe_2O_4$ was selected in the subsequent experiments.

3.2.2 Effect of pH on photocatalytic degradation of OTC. Since the species of OTC are changed critically with pH values (pH = 2: H_3OTC^+; pH = 5.5: $H_3OTC^\pm$; pH = 8.5: $HOTC^-$ and pH = 11.0: OTC^{2-}),[29] the effect of initial pH on photocatalytic degradation of OTC was investigated under visible light (Fig. 7(a)). For comparison, the results using TiO_2 (P25) and pure $CoFe_2O_4$ as photocatalysts are also given in Fig. 7(a). The photocatalytic degradation of OTC increased with pH from 2.0 to 8.5, but significantly reduced at pH = 11.0. It could be well explained by pH-dependent zeta potential of $0.3S-CoFe_2O_4$ shown in Fig. 7(b). From the figure, the PZC of $0.3S-CoFe_2O_4$ is between 9 to 10. At pH = 11 or at pH = 2, 5.5, electro-static repulsion is produced due to the similarly charged
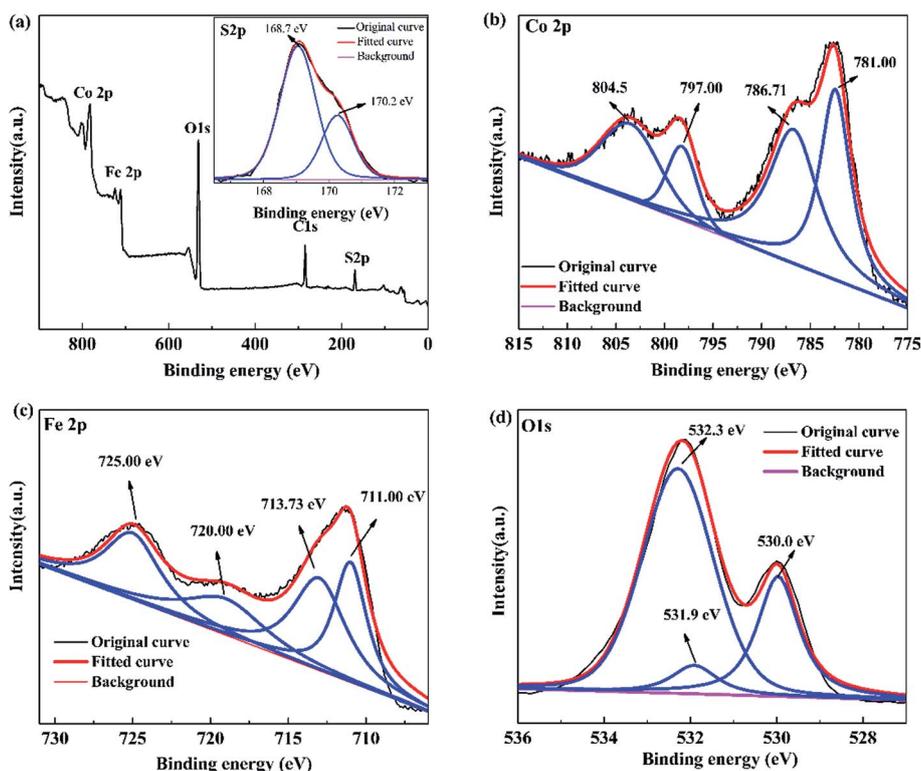

Fig. 5 XPS spectra of $0.3S-CoFe_2O_4$: (a) XPS survey, inset shows S 2p XPS spectra; (b) Co 2p, (c) Fe 2p, and (d) O 1s XPS spectra.
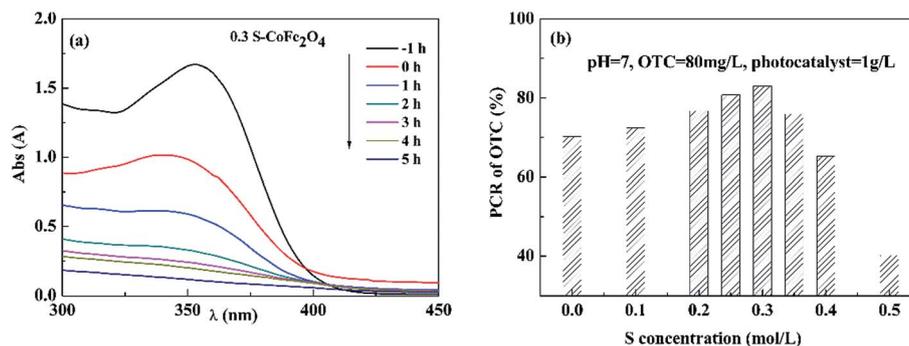
Fig. 6 (a) Typical UV-vis spectra changes of OTC solution with reaction time using 0.3S-CoFe$_2$O$_4$ as photocatalyst under visible light; (b) effect of S content on PCR of OTC after 5 h irradiation under visible light.

nanoparticle surface and species of OTC, which reduces surface absorption and leads to lower degradation efficiency. At pH = 8.5, OTC acts as HOTC$^-$, which can be easily adsorbed on the positive charged surface, and increases the conversion of OTC.

Moreover, the photocatalytic degradation kinetic process of OTC could be well described by the pseudo-first-order kinetic model ($-\ln C/C_0 = kt$) as shown in Fig. 7(c), where C_0 is the initial concentration of OTC, C is the concentration of OTC at time t, and k is the rate constant. As listed in Table 2, at pH = 8.5 the highest rate constant is 0.3358 h^{-1}, while the maximum conversion ratio of OTC reached to 89.4%.

Fig. 7(d) presents the variation of the total organic carbon (TOC) in aqueous solution with irradiation time, it can be observed that the TOC concentration declined with the degradation of OTC, and dropped to 23.2% after 5 h irradiation. The

Table 2 The pseudo-first order kinetic equations, rate constants (k) and regression coefficients (R^2) of photocatalytic degradation of OTC over S-CoFe$_2$O$_4$ at different pH

pH	The first order kinetic equation	k (h^{-1})	R^2
2	$-\ln(C/C_0) = 0.0284t$	0.0284	0.955
5.5	$-\ln(C/C_0) = 0.0572t$	0.0572	0.974
8.5	$-\ln(C/C_0) = 0.3358t$	0.3358	0.997
11	$-\ln(C/C_0) = 0.1073t$	0.1073	0.964

result suggested that the complete degradation of OTC to mineral end-products may be achieved using photocatalytic technology.
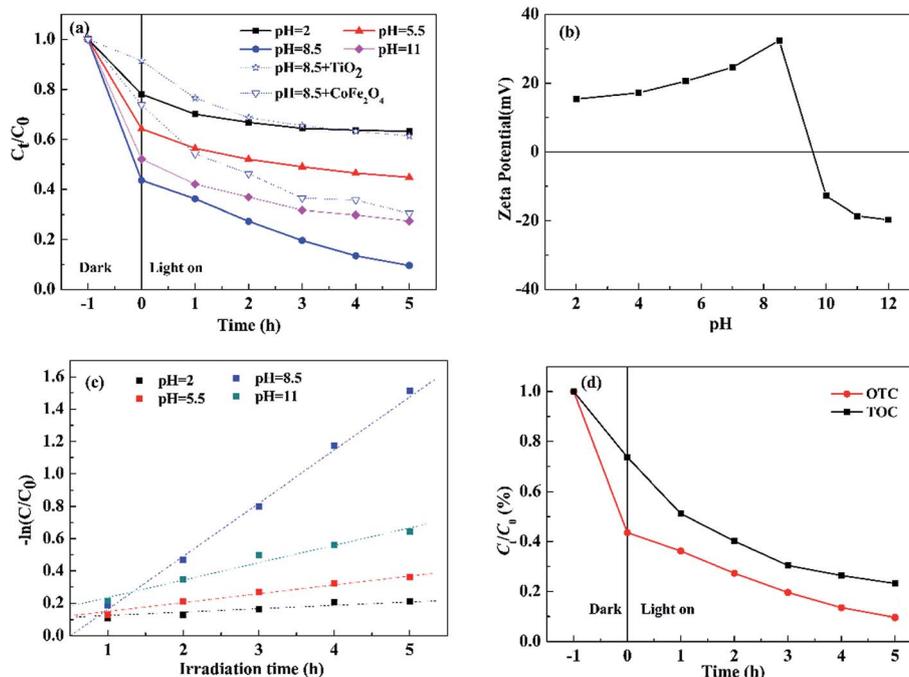

Fig. 7 (a) Effect of pH on photocatalytic degradation of OTC over 0.3S-CoFe$_2$O$_4$; (b) zeta-potential of aqueous dispersions of 0.3S-CoFe$_2$O$_4$ at different pH values; (c) Pseudo-first-order kinetic model fits the degradation kinetic curves of OTC; (d) remove efficiency changes of TOC and OTC with irradiation time in the presence of 0.3S-CoFe$_2$O$_4$ under visible light.
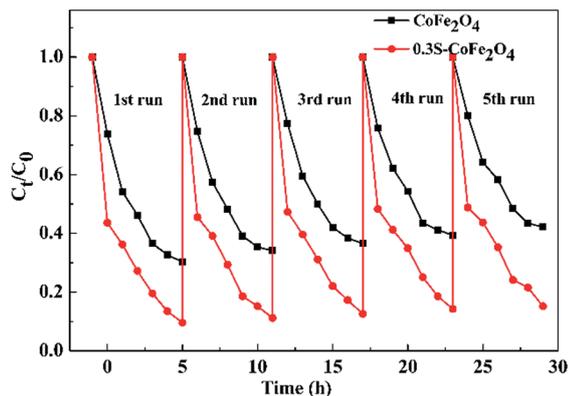
Fig. 8 Recyclability of 0.3S-CoFe$_2$O$_4$ for OTC degradation.

3.2.3 Reusability of 0.3S-CoFe$_2$O$_4$. The catalytic stabilities of CoFe$_2$O$_4$ and 0.3S-CoFe$_2$O$_4$ are tested upon separation of the photocatalysts magnetically, and their performance for each cycle is shown in Fig. 8. The PCR of OTC decreased from 90.4% to 84.8% after 5 cycles for 0.3S-CoFe$_2$O$_4$, while from 70.6% to

57.8% for CoFe$_2$O$_4$. This result showed that 0.3S-CoFe$_2$O$_4$ exhibited better photocatalytic stability and recoverability, because less photocatalyst lost during the separation progress due to its stronger magnetism. The slight decrease in PCR might attribute to the residual catalytic products absorbed on the surface of photocatalyst, which reduced the contact area between catalyst and pollutant.

3.3 Photocatalytic degradation pathway of OTC

The identification of intermediate products are carried out by LC/MSD SL, and iron spectra at different retention time (RT) of OTC solution after photocatalytic degradation for 1 h, 3 h and 5 h are presented in ESI Scan (Fig. S1†).

The iron spectra at RT = 5.527 and 1.455 min were detected in the solution after 1 h photocatalytic degradation. The main product ions at m/z 461.2 ([M + H]$^+$), m/z 145.0 ([M + Na]$^+$) might be identified as C$_{22}$H$_{24}$N$_2$O$_9$ (OTC) and C$_7$H$_6$O$_4$ (P6).[30] After 3 h photocatalytic degradation, three irons spectra at RT = 14.749, 13.066 and 1.455 min were detected in the solution. The main product ions at 381.3 ([M + H]$^+$), m/z 339.2 ([M + H]$^+$) and m/z 145.0 ([M + Na]$^+$) might be identified as C$_{21}$H$_{20}$N$_2$O$_5$ (P2),
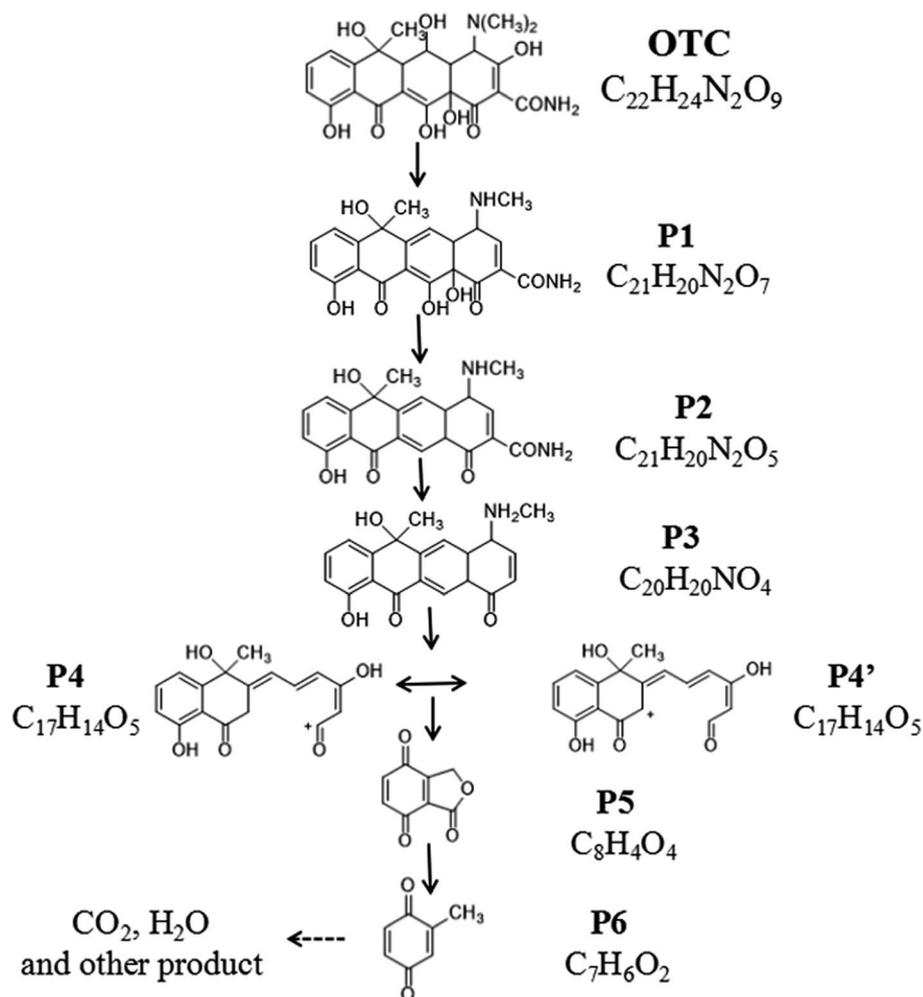

Fig. 9 Proposed degradation pathways of OTC.

$C_{20}H_{20}NO_4$ (P3) and $C_7H_6O_4$ (P6).[31] At RT = 15.444, 12.073 and 1.505 min, four main products at m/z 413.3 ($[M + H]^+$), m/z 299.2 ($[M + H]^+$), m/z 187.0 ($[M + Na]^+$) were detected after 5 h photocatalytic degradation, which might be identified as $C_{21}H_{20}N_2O_7$ (P1), $C_{17}H_{15}O_5$ (P4 or P4′) and $C_8H_4O_4$ (P5).[32] Based on the molecular weight and previous report. The possible photocatalytic degradation pathways of OTC are proposed and shown in Fig. 9.

3.4 Mechanism of photocatalysis
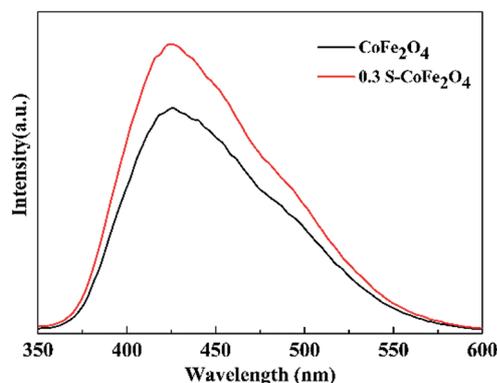
Fluorescence signal intensity of TAOH over $CoFe_2O_4$ and 0.3S-$CoFe_2O_4$ after visible light irradiation are presented in Fig. 10. The stronger fluorescence signal for 0.3S-$CoFe_2O_4$ meant lower level of recombination and the longer lifetimes of the carriers than $CoFe_2O_4$ nanoparticles,[33] then more valid e^-–h^+ pairs participated in the radical-chain reaction and more ·OH groups were generated.

In order to investigate the photocatalytic degradation mechanism of OTC, the trapping experiments of 0.3S-$CoFe_2O_4$ were performed to explore the main reactive species. CCl_4 (under sparging N_2), EDTA-2Na and t-BuOH served as $O_2^{·-}$, hole (h^+) and hydroxyl radical (·OH) scavenger, respectively. The different influences on photocatalytic degradation were observed in Fig. 11. CCl_4 and t-BuOH showed the significant reduce in PCR of OTC, dropped by 42.5% and 32.4% compared with the blank value, while EDTA-2Na almost inhibited the photocatalytic degradation process. The results suggested that photogenerated holes were the key active oxidizing species involved in the photocatalytic process, however $O_2^{·-}$ and ·OH also participated in the photocatalytic reaction.

The mechanism of OTC degradation can be described as the eqn (2)–(6). Firstly, in the solution, OTC molecules were adsorbed onto the surface of 0.3S-$CoFe_2O_4$. Under the visible light irradiation, conduction band electron (e^-) and valence band holes (h^+) are generated in 0.3S-$CoFe_2O_4$ bulk, then diffuse to the surface and react with H_2O and O_2 molecules adsorbed there to form reactive oxygen species (ROS), such as ·OH radical and $·O_2^-$. The ROS and h^+ can oxidize most of TC antibiotics to the mineral-end products.
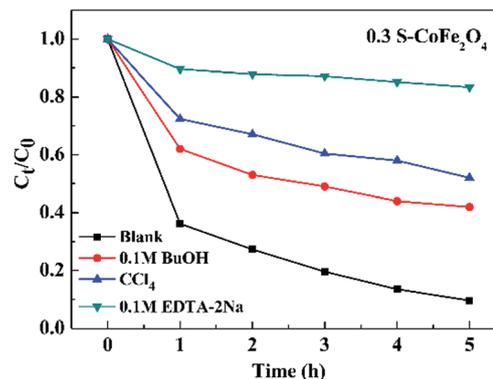
Fig. 11 Effect of different scavengers on the OTC degradation in the presence of 0.3S-$CoFe_2O_4$.

$$0.3S\text{-}CoFe_2O_4 + OTC \rightarrow (0.3S\text{-}CoFe_2O_4) - OTC \quad (2)$$

$$0.3S\text{-}CoFe_2O_4 + h\nu \rightarrow 0.3S\text{-}CoFe_2O_4 \ (e^- + h^+) \quad (3)$$

$$e^- + O_2 \rightarrow ·O_2^- \quad (4)$$

$$h^+ + H_2O \rightarrow ·OH + H^+ \quad (5)$$

$$OTC + ·OH/·O_2^-/h^+ \rightarrow \text{intermediate products} \rightarrow CO_2\uparrow + H_2O \quad (6)$$

Previous experiments showed that S might be doped in the bulk of $CoFe_2O_4$ lattice as S^{6+} and S^{2-}. The substitution of metal ion by S^{6+} may create an intra-band-gap state between VB and near to the CB edges that encourages the visible-light absorption,[20] while the anionic S doping into the lattice structure generates more oxygen defects and shifts the absorption edge in the visible-light region.[34] Thus, 0.3S-$CoFe_2O_4$ had narrower band gap and higher absorption rate for visible light than pure $CoFe_2O_4$. Besides, this impurity band hold on photoinduced e^- for more time to reduce the recombination rate, promoting more photoinduced h^+ to produce active radicals (hydroxyl and peroxide).

4. Conclusion

Sulfur-doped $CoFe_2O_4$ nanopowders with various content of S were synthesized using a simple calcining process. The effects of S doping on magnetism and photocatalytic activity under visible light have been studied, and 0.3S-$CoFe_2O_4$ exhibited the best comprehensive performance. The characterization results showed that introduction of S narrowed the band gap of 0.3S-$CoFe_2O_4$ and increased the absorption of the visible light. The optimized pH for OTC degradation was 8.5 due to the surface adsorption, and the maximum PCR could reach to 90.4% after 5 h visible light irradiation. 0.3S-$CoFe_2O_4$ also showed excellent recoverability, the PCR reached 84.8% at the fifth cycle. Seven intermediate products were detected after photocatalytic degradation, among these, P5 and P6 might suggest a partial ring-ruptured process, indicating the complete degradation of OTC to mineral end-products. Hole isolated from photocatalyst

Fig. 10 Fluorescence signal intensity of TAOH over $CoFe_2O_4$ and 0.3S-$CoFe_2O_4$ after visible light irradiation.

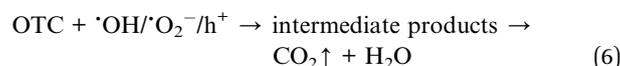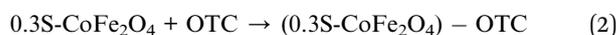played key role in oxidative degradation of OTC, while $^{\bullet}O_2^-$ and $^{\bullet}OH$ also participated the oxidative reactions.

Conflicts of interest

There are no conflicts to declare.

Acknowledgements

References

1 Y. Hong, C. Li, G. Zhang, Y. Meng, B. Yin, Y. Zhao and W. Shi, *Chem. Eng. J.*, 2016, **299**, 74–84.

2 J. B. Chen, Y. Wang, Y. J. Qian and T. Y. Huang, *J. Hazard. Mater.*, 2017, **335**, 117–124.

3 A. J. Watkinson, E. J. Murby, D. W. Kolpin and S. D. Costanzo, *Sci. Total Environ.*, 2009, **407**, 2711–2723.

4 N. Barhoumi, H. O. Vargas, N. Oturan, D. Huguenot, A. Gadrie, S. Ammare, E. Brillasd and M. A. Oturanb, *Appl. Catal., B*, 2017, **209**, 637–647.

5 R. Li, Y. Jia, J. Wu and Q. Zhen, *RSC Adv.*, 2015, **5**, 40764–40771.

6 F. L. Zhang, Q. Y. Yue, Y. Gao, B. Gao, X. Xu, Z. Ren and Y. Jin, *Chemosphere*, 2017, **182**, 483–490.

7 A. Y. Zhang, Y. Y. He, T. Lin and N. H. Huang, *J. Hazard. Mater.*, 2017, **330**, 9–17.

8 Q. Chen, S. Wu and Y. Xin, *Chem. Eng. J.*, 2016, **302**, 377–387.

9 J. Xue, S. Ma, Y. Zhou and Z. Zhang, *RSC Adv.*, 2015, **5**, 18832–18840.

10 D. Zhang, X. Pu, Y. Gao and C. Su, *Mater. Lett.*, 2013, **113**, 179–181.

11 K. Tezuka, M. Kogure and Y. J. Shan, *Catal. Commun.*, 2014, **48**, 11–14.

12 S. Sun, X. Yang, Y. Zhang, F. Zhang, J. Ding, J. Bao and C. Gao, *Prog. Nat. Sci.: Mater. Int.*, 2012, **22**, 639–643.

13 F. Miao, Z. Deng, X. Lv and G. Gu, *Solid State Commun.*, 2010, **150**, 2036–2039.

14 D. Moitra, M. Chandel, B. K. Ghosh and R. K. Jani, *RSC Adv.*, 2016, **6**, 76759–76772.

15 M. Saha, S. Mukherjee, S. Kumar and S. Dey, *RSC Adv.*, 2016, **6**, 58125–58136.

16 T. Prabhakaran, R. V. Mangalaraja, J. C. Denardin and J. A. Jiménez, *Ceram. Int.*, 2017, **43**, 5599–5606.

17 Y. Yao, G. Wu, F. Lu, S. Wang, Y. Hu, J. Zhang, W. Huang and F. Wei, *Environ. Sci. Pollut. Res.*, 2016, **23**, 21833–21845.

18 S. Singh and K. Neeraj, *Mater. Lett.*, 2015, **161**, 64–67.

19 H. Y. He and J. Lu, *Sep. Purif. Technol.*, 2017, **172**, 374–381.

20 S. A. Bakar and C. Ribeiro, *J. Mol. Catal. A: Chem.*, 2016, **421**, 1–15.

21 Q. Guo, Z. Zhang, X. Ma, K. Jing, M. Shen, N. Yu, J. Tang and D. D. Dionysiou, *Sep. Purif. Technol.*, 2017, **175**, 305–313.

22 D. Cao, X. Wang, L. Pan and H. Li, *J. Mater. Chem. C*, 2016, **4**, 951–957.

23 X. J. Guo, H. R. Li and S. G. Zhao, *J. Taiwan Inst. Chem. Eng.*, 2015, **55**, 90–100.

24 Y. H. Lin, H. T. Hsueh, C. W. Chang and H. Chu, *Appl. Catal., B*, 2016, **199**, 1–10.

25 Z. Yang, Z. Zhang, Y. Jiang, M. Chi, G. Nie, X. Lu and C. Wang, *RSC Adv.*, 2016, **6**, 33636–33642.

26 S. Singh and N. Khare, *RSC Adv.*, 2015, **5**, 96562–96572.

27 Z. P. Zhou, Y. Zhang and Z. Y. Wang, *Appl. Surf. Sci.*, 2008, **254**, 6972–6975.

28 S. Lee, J. S. Kang, K. T. Leung, W. Lee, D. Kim, S. Han, W. Yoo, H. J. Yoon, K. Nam and Y. Sohn, *J. Ind. Eng. Chem.*, 2016, **43**, 69–77.

29 S. A. Sassman and L. S. Lee, *Environ. Sci. Technol.*, 2005, **39**, 7452–7459.

30 Q. H. Chen, S. N. Wu and Y. J. Xin, *Chem. Eng. J.*, 2016, **302**, 377–387.

31 Z. Lu, P. Huo, Y. Luo, X. Liu, D. Wu, X. Gao, C. Li and Y. Yan, *J. Mol. Catal. A: Chem.*, 2013, **378**, 91–98.

32 N. Shao, J. N. Wang, D. D. Wang and P. Corvini, *Appl. Catal., B*, 2017, **203**, 964–978.

33 E. Jimenez-Relinque and M. Castellote, *Cem. Concr. Res.*, 2015, **74**, 108–115.

34 M. Harb, P. Sautet and P. Raybaud, *J. Phys. Chem. C*, 2013, **117**, 8892–8902.